NREL
NATIONAL RENEWABLE ENERGY LABORATORY

Investigation of Thermal Interface Materials Using Phase-Sensitive Transient Thermoreflectance Technique

Preprint

Xuhui Feng, Charlie King, Doug DeVoto, Mark Mihalic, and Sreekant Narumanchi

Presented at ITherm 2014
Orlando, Florida
May 27 – 30, 2014

NREL is a national laboratory of the U.S. Department of Energy
Office of Energy Efficiency & Renewable Energy
Operated by the Alliance for Sustainable Energy, LLC

This report is available at no cost from the National Renewable Energy Laboratory (NREL) at www.nrel.gov/publications.

Conference Paper
NREL/CP-5400-61106
August 2014

Contract No. DE-AC36-08GO28308

NOTICE

This report is available at no cost from the National Renewable Energy Laboratory (NREL) at www.nrel.gov/publications.

Available electronically at http://www.osti.gov/scitech

Available for a processing fee to U.S. Department of Energy and its contractors, in paper, from:

U.S. Department of Energy
Office of Scientific and Technical Information
P.O. Box 62
Oak Ridge, TN 37831-0062
phone: 865.576.8401
fax: 865.576.5728
email: mailto:reports@adonis.osti.gov

Available for sale to the public, in paper, from:

U.S. Department of Commerce
National Technical Information Service
5285 Port Royal Road
Springfield, VA 22161
phone: 800.553.6847
fax: 703.605.6900
email: orders@ntis.fedworld.gov
online ordering: http://www.ntis.gov/help/ordermethods.aspx

Cover Photos: (left to right) photo by Pat Corkery, NREL 16416, photo from SunEdison, NREL 17423, photo by Pat Corkery, NREL 16560, photo by Dennis Schroeder, NREL 17613, photo by Dean Armstrong, NREL 17436, photo by Pat Corkery, NREL 17721.

Investigation of Thermal Interface Materials Using Phase-Sensitive Transient Thermoreflectance Technique

Xuhui Feng, Charlie King, Doug DeVoto, Mark Mihalic, and Sreekant Narumanchi
National Renewable Energy Laboratory
Golden CO 80401
Email: xuhui.feng@nrel.gov

ABSTRACT

With increasing power density in electronics packages/modules, thermal resistances at multiple interfaces are a bottleneck to efficient heat removal from the package. In this work, the performance of thermal interface materials such as grease, thermoplastic adhesives and diffusion-bonded interfaces are characterized using the phase-sensitive transient thermoreflectance technique. A multi-layer heat conduction model was constructed and theoretical solutions were derived to obtain the relation between phase lag and the thermal/physical properties. This technique enables simultaneous extraction of the contact resistance and bulk thermal conductivity of the TIMs. With the measurements, the bulk thermal conductivity of Dow TC-5022 thermal grease (70 to 75 μm bondline thickness) was 3 to 5 W/(m·K) and the contact resistance was 5 to 10 mm^2·K/W. For the Btech thermoplastic material (45 to 80 μm bondline thickness), the bulk thermal conductivity was 20 to 50 W/(m·K) and the contact resistance was 2 to 5 mm^2·K/W. Measurements were also conducted to quantify the thermal performance of diffusion-bonded interface for power electronics applications. Results with the diffusion-bonded sample showed that the interfacial thermal resistance is more than one order of magnitude lower than those of traditional TIMs, suggesting potential pathways to efficient thermal management.

KEY WORDS: Thermal interface materials, phase-sensitive transient thremoreflectance, contact resistance, bulk thermal conductivity, thermophysical properties

NOMENCLATURE

c	specific heat, J/(kg·K)
d	thickness, m
f	frequency, Hz
h	contact conductance, W/(m^2·K)
k	thermal conductivity, W/(m·K)
l_p	thermal penetration depth, m
q_0	amplitude of laser heat flux
r	radial axis, m
R	thermal resistance, m^2·K /W
t	time, s
T	temperature, K
z	axis along thickness direction, m

Greek symbols

α	thermal diffusivity (m^2/s)
ω	angular frequency (radians/s)
ρ	density (kg/m^3)

Subscripts

1, 2, 3	layer index in multi-layer modeling

INTRODUCTION

With increasing power density in electronics packages/modules, the need for efficient heat removal is becoming important. Thermal interface materials (TIMs) are of particular interest in packaging and play a key role in reducing the thermal resistance between mating surfaces in the heat conduction path [1-6]. Effective TIMs reduce the package resistance and help maintain an appropriate working temperature to ensure both performance and reliability of the devices. To fulfill the purpose of efficient conduction of heat, TIMs usually are expected to possess two major characteristics: high thermal conductivity and good conformability to mating surfaces. Commercially available TIMs include thermal grease, gels, solders, and phase-change materials (PCMs). Significant amount of research has been reported regarding the synthesis, properties, and modifications of TIMs. Liu and Chung used scanning calorimetry to evaluate PCMs for use as TIMs [7]. Aoyagi *et al.* [8] evaluated the polyol-based PCMs, which have thermal contact conductance higher than those of paraffin wax, polyether glycol, etc. Its thermal stability is superior to other PCMs [8]. Boron nitride is used as it is more effective than carbon black. Aoyagi and Chung [9] reported antioxidant-based PCMs with high thermal stability. Yu *et al.* [10] applied graphite nanoplatelets as filler for epoxy composites and found that the thermal conductivity was enhanced with a relatively low volume fraction due to the filler's high aspect ratio, two-dimensional geometry, and low thermal interface resistance. In addition, for new nanostructured materials that may possess improved thermal and mechanical properties, their potential of being applied as TIMs is also studied. Cross *et al.* [11] measured the thermal performance of dense, vertically aligned multi-wall carbon nanotube (MWCNT) arrays as TIMs. CNTs were utilized as TIMs after appropriate metallization and bonding. The thermal resistance was measured using a photoacoustic technique to be in the range of 1.7 to 10 mm^2·K/W, depending on the vertical length of CNTs.

To experimentally characterize the thermal properties and thermal performance of TIMs, a variety of techniques have been developed and utilized, including both steady-state and transient techniques. Lasance[12] reviewed several urgent needs for developing widely accepted test methods of TIMs due to the substantial difference amongst TIMs. There can be significant discrepancies in the results obtained from the various techniques. But in recent years, the ASTM D-5470 [13] has emerged as a standard based on a steady-state approach. In addition, a number of steady-state and transient cannot accurately measure thermal resistances below 1 mm^2·K/W. Culham *et al.* [14] designed a test apparatus that exceeded all specifications stipulated in ASTM-D5470-95 and that can be used to characterize TIMs. Xu and Fisher [15] tested the thermal conductance of silicon wafers with CNT arrays using a

one-dimensional steady-state heat conduction experiment with a reference calorimeter setup. Chen *et al.* [16] designed a platform based on ASTM D5470 test method to measure polymeric TIMs such as greases. Due to the limitations of ASTM–D5470 measurements, such as sample scale, response time, and relatively low temperature measurement resolution, transient techniques are being increasingly used to characterize the thermal properties of small-scale materials, which are widely adopted in micro/nano-electronics. Compared with steady-state techniques, transient characterization has competitive advantages in response time, precision, and small-scale measurements [17-20]. Of all the transient techniques, transient thermoreflectance (TTR) has been extensively used in characterizing the thermal/optical properties of thin film materials [21-25]. Ohsone *et al.* [23] performed optical measurement of thermal contact conductance between thin, solid films and also established a configuration of frequency-domain thermoreflectance experiment. This experiment was then modified by Tong *et al.* [26] to study CNTs as novel interface materials. In addition to frequency-domain TTR, Lyeo and Cahill [25] used time-domain TTR to measure the thermal conductance between highly dissimilar materials. They concluded that coupling electrons in a metal to phonons in a dielectric substrate does not significantly contribute to thermal transport at interfaces. Komarov and Raad [24] analyzed the performance of the TTR method for measuring the thermal conductivities for various materials.

In this work, we mainly focus on TIMs which could be applicable for power electronics packaging applications. Narumanchi *et al.* [27] briefly reviewed the state of the art of TIMs in power electronics applications. In automotive power electronics, it is critical to have efficient heat removal to keep device temperature under limits, assure high reliability and lower the cost of components. In a power electronics package, the thermal resistance of interface materials depends on both the thermal conductivity of the fillers and also the conformability to mating surfaces. When a TIM is applied, the bondline thickness (BLT) is usually as thin as tens of micrometers, and the thermal conductivity of this scale is expected to be smaller than its bulk value. Also, because of the non-ideal surface contact and adhesion, the interface emerges as a significant hindrance to heat removal. Therefore, study of the thermal conductivity and contact resistance simultaneously aids in understanding the impacts from these factors, thus improving the synthesis of TIMs. In addition, for very low thermal resistance materials (< 1 $mm^2 \cdot K/W$), some of the conventional steady-state (e.g. ASTM-D5470) and transient (e.g. xenon flash) techniques are inadequate. For these reasons, we developed a laser-based phase-sensitive TTR (PSTTR) technique and performed measurements on different TIMs to derive their thermophysical properties. The experimental method is briefly introduced and principles of PSTTR are presented. Heat transfer modeling and corresponding theoretical analysis are then described, along with applicable solutions of phase lag used to fit parameters of interest. Measurement results and discussions are presented along with sensitivity and uncertainty analysis.

EXPERIMENTATION

Sample Preparation

We studied four test articles in this work to determine their thermophysical properties when used as thin bonding layers. A plain 100 μm thick silicon wafer was used for baseline measurement and calibration. A variety of commercial and advanced TIMs were chosen to synthesis the layered samples. The first layered sample we fabricated was composed of Dow Corning TC-5022 thermal grease sandwiched between two 100 μm thick silicon wafers. After cleaning the surface, a small quantity of TC-5022 was applied to one wafer, and the second wafer was pressed onto the grease and squeezed to cause the grease to flow between the two wafers. The samples were further annealed under elevated temperature and under pressure to create the possibly smallest layer of grease. Typical grease layer thickness of 60 to 70 μm was achieved, in accordance with those of most BLTs of thermal greases. This sample represents a standard commercial method of creating thermal contact between cold plates and electronic components.

The second layered sample for TIM study was made by bonding two plain silicon wafers using Btech thermoplastic film (HM-2, from Btech Corp.). The film is a composite of high-density graphic fibers mixed with high temperature adhesive. Btech thermoplastic film was chosen because the highly aligned fibers are intended to provide enhanced out-of-plane thermal conduction between the hot component and the cooling media. The sample was assembled similarly to the one bonded using Dow thermal grease. A piece of film was placed between two 150 μm thick silicon wafers and bonded together using force and heat per the manufacturer's recommendations. A Btech material thickness of about 60 μm was achieved.

Among emerging new classes of high-performance bonding techniques, diffusion bonding is a promising one in wafer bonding as it removes physical interface materials to enhance the heat dissipation. The diffusion-bonded silicon samples on which measurements were performed in this work were synthesized by our collaborators (Delphi). A microscopic image of the bondline is shown in Fig. 1, with thickness marked for two silicon wafers.

Phase-sensitive transient thermoreflectance

Experiment setup of PSTTR. The configuration of the PSTTR technique is presented in Fig. 2. The pump laser is modulated using a wheel chopper at a particular frequency, f, and then is focused onto the front surface of the sample. The absorption of this energy at the front surface generates a thermal wave traveling through the sample, inducing temperature fluctuation of the same frequency f on the back surface. A probe laser is focused to detect the small temperature fluctuation.

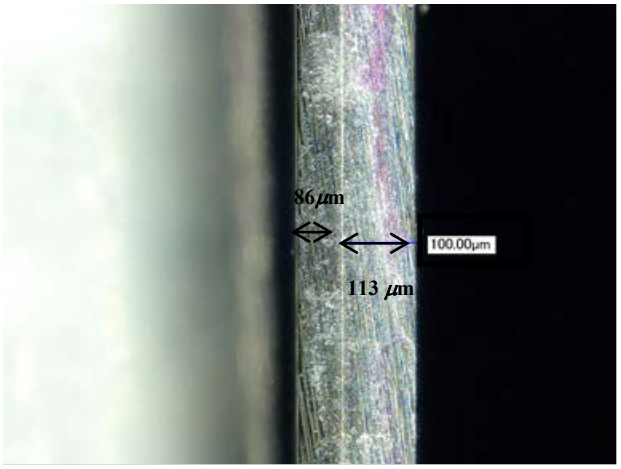

Fig. 1 Microscopic side view of diffusion-bonded sample; the thicknesses of the two bonded silicon wafers are shown.

Within a small range of temperature variation, namely, 10 degrees, the coefficient of thermoreflectance is assumed constant and the reflectivity change is linearly proportional to temperature change. Thermoreflectance describes a surface's ability to reflect an optical signal and is highly dependent on the materials and also the wavelength of the optical signals. A photodiode is used to receive the reflected probe laser and then the converted electrical signal is transmitted to a lock-in amplifier. By comparing it with a reference input from the pump laser modulation, the lock-in amplifier extracts the amplitude and phase information of the signal at the frequency *f*. Because the amplitude depends on many factors, such as the power of the laser heating, laser spot size, and surface properties, most of which are not documented in literatures, the theoretical predication of the amplitude faces many unknowns and uncertainties. Contrarily, the phase of the signal is independent of these parameters and only depends on the thermal properties of the sample, e.g., the thermal conductivity of the materials, thermal conductance of interfaces, etc. Hence, the phase information of the reflected signal is chosen over the amplitude to derive the thermal properties based on the corresponding heat transfer modeling.

The apparatus for this technique is also shown in Fig. 2. Heating is provided by a diode laser (pump laser) at a wavelength of 808 nm and a maximum power of 5W. The continuous laser signal is then modulated by an optical chopper. The modulation frequency is controlled by a waveform generator (Picotest G5100A), which also output the same frequency into the lock-in amplifier as a reference input. The heating laser is focused onto the surface with a spot radius of approximately 1.5 mm, yielding a maximum flux of about 2.83 W/mm^2. Another diode laser of 405-nm wavelength and much reduced power of about 5 mW is employed as the probe laser. The spot size of the probe laser is about 0.3 mm radius, small enough compared with the spot size of pump laser. Therefore, the probe laser is simply used to detect the temperature variation without introducing a thermal effect to the temperature field. A Gallium Phosphide (GaP) photodiode (Thorlab DET-25K) is connected to a 20KΩ resistor by amplifying the photodiode signal into a lock-in amplifier (SR850, Stanford Research System). During each measurement, a series of frequencies is generated, and then the pump-probe process is conducted at each frequency. A LabView data acquisition system is used to automatically complete the whole measurement.

Among many factors that may affect this experiment, the alignment of two laser signals is most critical, as it strongly influences the strength of signal into the photodiode. Both the pump and probe lasers are mounted on motorized stages, ensuring accurate adjustment of each spot. The probe laser spot is first fixed and marked using a charge-coupled device (CCD) camera. The pump laser is then fine-tuned using the motorized stages to identify the best alignment by observing the intensity readings of the lock-in amplifier. This alignment process is usually delicate and difficult due to the small but oscillating temperature response on the back surface. In addition, the appropriate ratio between the two spot sizes is important for the success of the experiment.

Based on a comparison between the photodiode signal and a reference input of the modulation frequency, phase reading from the lock-in amplifier represents a backward shift from the original periodic waveform. Therefore, it is defined as a phase lag in this work. This phase lag is not only composed of the effect of the thermal transport in the sample, but also that from the devices and equipment used in the experiment. Therefore, a calibration is required so that the systematic and environmental effects can be qualitatively determined. Towards this end, the experiment is first run at the same frequency series without mounting the sample, and the phase lag is recorded as a baseline. This baseline phase lag is subtracted from the phase lag data acquired from the sample. This systematic phase lag is usually consistent when the laser parameters change.

Theory of PSTTR. To extract thermal property information from the phase lag data, a transient heat transfer model is required to solve the temperature distribution in the multi-layer structure upon laser heating. In the simplest case, a one-dimensional model is studied first by assuming isotropic and temperature-independent thermal properties. The governing equation for one-dimensional heat transfer is:

$$\frac{1}{\alpha}\frac{\partial T}{\partial t} = \frac{\partial^2 T}{\partial z^2} \quad (1)$$

where T is the temperature, α is the thermal diffusivity, t is the time and z is the spatial coordinate.

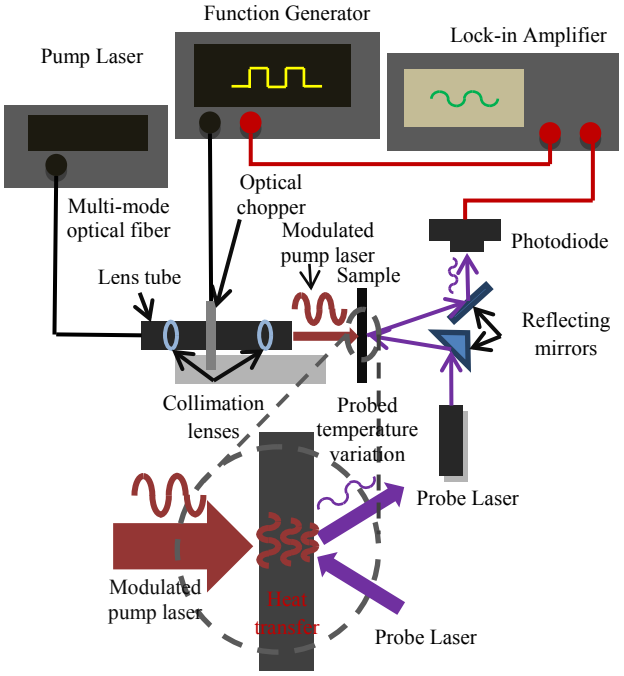

Fig. 2 Experimental configuration of the phase-sensitive transient thermoreflectance technique

Using the separation of variables method and a periodic heat source of angular frequency ω, a general solution of Eq. (1) is obtained as,

$$T(t,z) = e^{-i\omega t}\left(Ae^{(1-i)\frac{z}{\sqrt{2\alpha/\omega}}} + Be^{-(1-i)\frac{z}{\sqrt{2\alpha/\omega}}}\right)$$
$$= Ae^{\frac{z}{L_p}}e^{i(-\frac{z}{L_p}-\omega t)} + Be^{-\frac{z}{L_p}}e^{i(\frac{z}{L_p}-\omega t)}, \quad (2)$$

where the term $\sqrt{2\alpha/\omega}$ is defined as the thermal penetration depth, L_p, which denotes a length scale over which the thermal energy can propagate before getting substantially damped. If the thickness is significantly greater than the penetration depth, it is then assumed that the sample is relatively thick. By adopting a periodic heat flux $q_0e^{-i\omega t}$ with amplitude q_0 and frequency ω as the boundary condition at the front surface (z = 0), Eq. (2) is further derived as:

$$T(t,z) = \frac{q_0 L_p}{\sqrt{2}k}e^{-\frac{z}{L_p}}e^{i(\frac{z}{L_p}+\frac{\pi}{4}-\omega t)} \quad (3)$$

where k is the thermal conductivity. A phase lag of $\left(z/L_p + \pi/4\right)$ is identified between heat flux at the front surface and the temperature response on the back surface. It is seen from the Eq. (3) that the phase lag is only dependent on the thermal diffusivity α. Therefore, the phase lag is relatively robust compared with the amplitude when deriving the thermal properties. The derivation is achieved using a least-square fitting technique through the whole frequency range. A typical fitting plot for a silicon wafer is presented in the Results section.

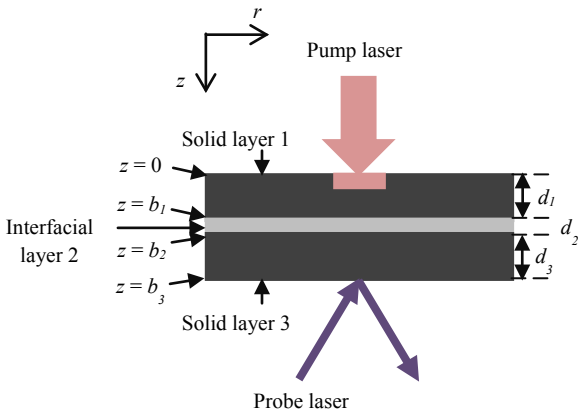

Fig. 3 Schematic of the multi-layer samples measured using PSTTR (not scaled).

Three-layer structure. Now we examine multilayer structures that are common in microelectronics/power electronics applications. A typical geometry is shown in Fig. 3. It contains two solid materials (1 and 3) and one interfacial layer (2). The properties of the three layers are indicated by subscripts 1, 2, and 3. To theoretically analyze the temperature field in a three-layer structure, an axial-symmetric three-layer transient heat transfer model is established as:

$$\frac{1}{\alpha_i}\frac{\partial T_i(r,z,t)}{\partial t} = \frac{1}{r}\frac{\partial}{\partial r}\left(r\frac{\partial^2 T_i(r,z,t)}{\partial r}\right) + \frac{\partial^2 T_i(r,z,t)}{\partial z^2}, \quad (4)$$

where the subscript i represents the ith layer (i = 1, 2, 3), as denoted in Fig. 3. Due to the geometric symmetry of the structure, only heat transfer occurring along the r and z directions is considered, indicated by the coordinate axes in this figure. In addition, heat loss from the surface to the surroundings is assumed to be negligible. Then the boundary conditions are as follows:

At z = 0, a periodic heat source of intensity q_0 and angular frequency ω are used:

$$q_0 f(r)e^{-i\omega t} = -k_1\frac{\partial T_1}{\partial z}; \quad (5\text{-}1)$$

at z = b_3, an insulation boundary condition is applied, due to the case that the thickness is large enough and also the Biot number is small:

$$k_3\frac{\partial T_3}{\partial z} = 0; \quad (5\text{-}2)$$

at z = b_1, which is interface 1, the energy balance is shown as:

$$-k_1\frac{\partial T_1}{\partial z}\Big|_{z=b_1} = h_{12}\left(T_1(b_1) - T_2(b_1)\right) = -k_2\frac{\partial T_2}{\partial z}\Big|_{z=b_1}; \quad (5\text{-}3)$$

The same boundary condition is also applied to interface 2 at z =b_2,

$$-k_2\frac{\partial T_2}{\partial z}\Big|_{z=b_2} = h_{23}\left(T_2(b_2) - T_3(b_2)\right) = -k_3\frac{\partial T_3}{\partial z}\Big|_{z=b_2}, \quad (5\text{-}4)$$

where k_1, k_2, and k_3 are the thermal conductivities of the respective layers; h_{12} and h_{23} are the contact conductance at the 1–2 interface and the 2–3 interface, respectively. $f(r)$ is the axial symmetric heating function that defines the heat flux distribution over the surface and is assumed to be uniform to simplify the analysis. The surface outside of the heating region

is insulated because the laser heating is localized and the geometry along the thickness direction is much smaller than that at the other directions.

This equation is solved by using the integral transform method [23]. After the Hankel transform and Laplace transform are implemented, the governing equation is converted as follows:

$$\frac{\partial^2 w_i(\lambda,z,s)}{\partial z^2} - \left(\lambda^2 + \frac{s}{\alpha_i}\right) w_i(\lambda,z,s) = 0, \quad (6)$$

where λ and s are the variables resulting from the Hankel and Laplace transforms, respectively. $w_i(\lambda, z, s)$ is the Hankel and Laplace transform of temperature function $T_i(r, z, t)$. Then, the general solution for the i-th layer is expressed as:

$$w_i(\lambda,z,s) = \tilde{A}_i cosh(\eta_i z) + \tilde{B}_i sinh(\eta_i z), \quad (7)$$

where $\eta_i = \sqrt{\lambda^2 + \frac{s}{\alpha_i}}$.

The boundary conditions are written as:

$$\frac{q_0}{s+i\omega}\int_{r=0}^{\infty} f(r)\cdot J_0(\lambda r)dr = -k_1 \left.\frac{\partial w_1}{\partial z}\right|_{z=0}, \quad (8\text{-}1)$$

$$-k_1 \left.\frac{\partial w_1}{\partial z}\right|_{z=b_1} = h_{12}(w_1 - w_2)|_{z=b_1} = -k_2 \left.\frac{\partial w_2}{\partial z}\right|_{z=b_2}, \quad (8\text{-}2)$$

$$-k_2 \left.\frac{\partial w_2}{\partial z}\right|_{z=b_2} = h_{23}(w_2 - w_3)|_{z=b_2} = -k_3 \left.\frac{\partial w_3}{\partial z}\right|_{z=b_3}, \quad (8\text{-}3)$$

$$-k_3 \left.\frac{\partial w_3}{\partial z}\right|_{z=b_3} = 0, \quad (8\text{-}4)$$

where $J_0(\lambda r)$ is the zeroth Bessel function, which represents the Hankel transform of the heating function. Coefficients $\tilde{A}_i$ and B_i are solved by substituting the general solution into boundary conditions. Then inverse transforms are used to recover the temperature distribution in real space.

Because only the temperature response on back surface is of interest, $r = 0$ and $z = b_3$ are chosen to retrieve the temperature distribution on the back surface. Under a high-frequency limit, the solution is simplified as:

$$T_3(0,b_3,t) = \frac{4q_0}{k_1\sqrt{\pi f/\alpha_1}} \cdot exp\left[-\left(d_1\sqrt{\frac{\pi f}{\alpha_1}} + d_2\sqrt{\frac{\pi f}{\alpha_2}} + d_3\sqrt{\frac{\pi f}{\alpha_3}}\right)\right] \frac{exp\left[i\left[\frac{\pi}{4} + d_1\sqrt{\frac{\pi f}{\alpha_1}} + d_2\sqrt{\frac{\pi f}{\alpha_2}} + d_3\sqrt{\frac{\pi f}{\alpha_3}} - \omega t\right]\right]}{\left[\begin{array}{c} 1+\sqrt{\frac{(k\rho c)_2}{(k\rho c)_1}}+\sqrt{\frac{(k\rho c)_3}{(k\rho c)_1}}+\sqrt{\frac{(k\rho c)_3}{(k\rho c)_2}}+(1-i)\frac{\sqrt{\pi f(k\rho c)_2}}{h_{12}}+(1-i)\frac{\sqrt{\pi f(k\rho c)_3}}{h_{12}}+ \\ (1-i)\frac{\sqrt{\pi f(k\rho c)_3}}{h_{23}}+(1-i)\sqrt{\frac{(k\rho c)_2}{(k\rho c)_1}}\frac{\sqrt{\pi f(k\rho c)_3}}{h_{23}}+(1-i)^2\frac{\sqrt{\pi f(k\rho c)_2}}{h_{12}}\frac{\sqrt{\pi f(k\rho c)_3}}{h_{23}} \end{array}\right]}, \quad (9)$$

where $d_1 = b_1$, $d_2 = b_2 - b_1$ and $d_3 = b_3 - b_2$, as seen in Fig. 3, denote the thickness of each layer. Thermophysical properties in each layer are summarized into one term $\sqrt{(k\rho c)_i}$, $i = 1, 2, 3$. This expression is defined as thermal effusivity, which is a measure of a material's ability to exchange thermal energy with its surroundings. Given that the thermal resistance R is the reciprocal of the thermal conductance h, the phase lag in the high-frequency limit can be then extracted as:

$$\emptyset = \frac{\pi}{4} + d_1\sqrt{\frac{\pi f}{\alpha_1}} + d_2\sqrt{\frac{\pi f}{\alpha_2}} + d_3\sqrt{\frac{\pi f}{\alpha_3}} + tan^{-1}\left[\frac{\left(\begin{array}{c}\sqrt{\pi f(k\rho c)_2}\cdot R_{12}+\sqrt{\pi f(k\rho c)_3}\cdot R_{12}+\sqrt{\pi f(k\rho c)_3}\cdot R_{23}+ \\ \sqrt{\frac{(k\rho c)_2}{(k\rho c)_1}}\cdot\sqrt{\pi f(k\rho c)_3}\cdot R_{23}+2\sqrt{\pi f(k\rho c)_2}\cdot R_{12}\cdot\sqrt{\pi f(k\rho c)_3}\cdot R_{23}\end{array}\right)}{\left(\begin{array}{c}1+\sqrt{\frac{(k\rho c)_2}{(k\rho c)_1}}+\sqrt{\frac{(k\rho c)_3}{(k\rho c)_1}}+\sqrt{\frac{(k\rho c)_3}{(k\rho c)_2}}+\sqrt{\pi f(k\rho c)_2}\cdot R_{12}+\sqrt{\pi f(k\rho c)_3}\cdot R_{12}+ \\ \sqrt{\pi f(k\rho c)_3}\cdot R_{23}+\sqrt{\frac{(k\rho c)_2}{(k\rho c)_1}}\cdot\sqrt{\pi f(k\rho c)_3}\cdot R_{23}\end{array}\right)}\right] \quad (10)$$

Eq. (10) expresses the phase lag at the back surface and is related to several key parameters, such as the thermophysical properties of each layer and also the contact resistances, which are of particular interest. With the theoretical phase lag and experimental data, the thermophysical properties can be precisely estimated using a multi-parameter fitting method.

Although the phase lag (Eq. (10)) is derived based on a three-layer heat transfer model, it is applicable to derive the temperature distribution in both two-layer and single-layer structures, with necessary assumptions for the thermal and physical properties. Note that in Eq. (10), if R_{12} and R_{23} approach 0, meaning an absence of interfaces, and all thermophysical properties are set to be identical, this equation reduces to the following form:

$$\emptyset = \frac{\pi}{4} + \sqrt{\frac{\pi f}{\alpha_1}}(d_1 + d_2 + d_3), \quad (11)$$

which is in exactly the same form as the phase lag in Eq. (3). Eq. (10) is also used to derive a solution for a two-layer structure. By applying similar assumptions that the contact resistance R_{12} is 0 and solid layer 1 and bonding layer 2 possess identical thermophysical properties, namely, $(k\rho c)_1 = (k\rho c)_2$, Eq. (10) further reduces to the following expression:

$$\emptyset = \frac{\pi}{4} + \sqrt{\frac{\pi f}{\alpha_1}}(d_1 + d_2) + d_3\sqrt{\frac{\pi f}{\alpha_3}} + tan^{-1}\left[\frac{\left(\sqrt{\pi f(k\rho c)_3}\cdot R_{23}\right)}{\left(1+\sqrt{\frac{(k\rho c)_3}{(k\rho c)_1}}+\sqrt{\pi f(k\rho c)_3}\cdot R_{23}\right)}\right]. \quad (12)$$

The solution of a two-layer structure is useful when studying a direct-bonded sample, which usually contains no physical bonding material, only a pure bond line.

This series of phase lag solutions for single-layer (Eq. (11)), two-layer (Eq. (12)) and three-layer (Eq. (10)) structures inspires us to conduct an in-depth study of heat transfer in a generic multi-layer structure. It is observed from these equations that all three solutions follow a certain regularity of contributions from different materials. A (π/4) term appears in all three equations, which represents an intrinsic phase lag caused by absorption of heat on the front surface, regardless of materials. Terms in the form of b/l_p indicate the phase lag caused by thermal wave propagation inside each layer. Contributions of the interfaces and thermophysical properties are included in the inverse tangential function. Following the same geometrical setting and analogous boundary conditions, a general N-layer model can be established and solved. The N-layer model solution provides a useful reference when a

complicated multi-layer sample is studied using optical heating and sensing techniques, such as PSTTR and laser flash. More details and derivations will be discussed in another paper.

RESULTS AND DISCUSSIONS

Single materials

To validate the experimental setup and confirm the accuracy of the technique, it is necessary to measure materials with documented properties. A single silicon wafer was first tested as a standard material because its thermal and physical properties are well studied. Silicon wafers of different thicknesses (100, 120, 150, 170, 270, and 280 μm) were tested using PSTTR. Typical phase lag–frequency data points are plotted in Fig. 4, in which a theoretical line is also added. As shown in Eq. (3), the phase lag is linearly dependent on the term b/L_p. with an intercept of $-\pi/4$. Therefore, in Fig. 4, if a normalized frequency is chosen as the x axis, measured points from silicon wafers of varied thicknesses all converge to close to the theoretical linear profile. If the thickness is too small so that the penetration depth is comparable or larger than the thickness, the front side phase lag and traveling wave phase lag both approaches 0, resulting an overall phase lag of ~ 0. Only when the thickness is large, the total phase lag is quantified as ($\pi/4+b/L_p$). [26] Therefore, to satisfy the thick-sample assumption, frequencies are carefully chosen to ensure the thermal penetration depth is smaller than the thickness. Usually the applicable frequency region is determined when the ratio b/l_p is greater than 0.8, which is defined as the high-frequency limit. The frequency determined by this limit assures that the phase lag at the front surface approaches $\pi/4$ and the contribution from the traveling thermal wave is b/l_p [23, 26]. From Fig. 4, the region of $b/l_p > 1.0$ is intentionally chosen for global fitting. The optimal agreement between the experimental data and the theoretical solution yields the best value for the thermal diffusivity for the tested silicon wafer. Taking a silicon wafer of 100 µm thickness for instance, the thermal diffusivity is fitted to be about 7.9×10^{-5} m^2/s. The density and specific heat of silicon are 2,230 kg/m^3 and 712 J/(kg·K), respectively, [28] thus, the thermal conductivity is calculated to be 131 W/(m·K), in good agreement with the generally documented value of 135 W/(m·K). [23] If the thickness varies, the derived thermal diffusivity does not show a significant change because the normalized frequency–phase curves at different thicknesses actually converge to the theoretical profile. Measurement results and parameters adopted in the fit are listed in Table 1, along with uncertainties for the fitted parameters, such as thermal conductivity, k, and thermal diffusivity, α.

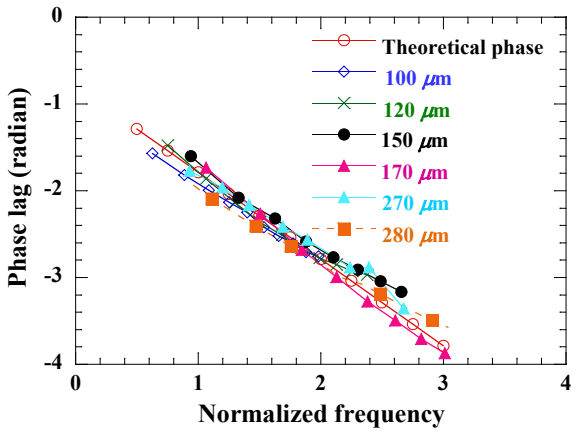

Fig. 4 Plot of experimental phase lags as a function of normalized frequency for plain silicon wafers of different thicknesses. The theoretical phase lag profile is also added for comparison.

Table 1. Parametric values for three different materials measured in this work using PSTTR. Uncertainties of fitted values are marked.

Parameters	Silicon wafer	TC-5022	Btech HM-2
Total Thickness (μm)	100	270	380
BLT (μm)		70	60
Density (kg/m^3)	2,330	3,230	1,520
Specific heat (J/(kg·K))	712	251	1,010
Thermal conductivity (W/(m·K))	131 ± 17.00	3.41 ± 0.34	37.53 ± 6.76
Thermal diffusivity ($\times 10^{-5}$ m^2/s)	7.90 ± 1.00	0.42 ± 0.04	2.44 ± 0.44
Contact resistance (mm^2·K/W)		8.74 ± 3.06	3.06 ± 1.07
Total thermal resistance (mm^2·K/W)		37.03 ± 6.40	7.49 ± 1.87

Thermal grease TC-5022

As a predominant TIM use in the automotive industry, thermal grease has been widely studied. However, the ASTM D5470 technique or the transient laser flash technique can only provide the overall interfacial thermal resistance without distinguishing the effects from the interface material and contacting surfaces. Therefore, an in-depth study to understand the thermal properties of each component would aid in improving the performance of thermal grease and the synthesis of other types of TIMs. The thermal grease measured in this work is Dow Corning TC-5022 material, and the fabrication details of the sample are introduced in a prior section. The

bound silicon wafers are studied as well, using PSTTR as stated above. Their geometrical, physical, and thermophysical properties are recorded and then used in the data analysis of three-layer sample measurement. The overall thickness is slightly different from spot to spot, varying from 60 to 70 μm. As analyzed above, the silicon-grease-silicon composite structure is a three-layer model, and Eq. (10) gives the phase lag in the high frequency region. In addition, Eq. (9) shows that the temperature oscillation at the back surface varies as $\left[-\left(d_1\sqrt{\frac{\pi f}{\alpha_1}}+d_2\sqrt{\frac{\pi f}{\alpha_2}}+d_3\sqrt{\frac{\pi f}{\alpha_3}}\right)\right]$, and it strongly depends on the thermophysical properties and also the frequencies. Therefore, if the modulation frequency is increased, the temperature response on the back surface will decrease exponentially. This is also observable from the lock-in amplifier readings. Thus, to assure a signal strong enough to suppress the environmental disturbance, the frequency range chosen is from 2 to 4 kHz. In Fig. 5, typical phase lag data for TC-5022 is plotted out against the normalized frequency. The results from theoretical modeling are also added for comparison. The *x*-axis is the normalized frequency, which summarizes the traveling wave contribution in each layer. As seen, the measured data points show some oscillation but are still very close to the theoretical results. Because the PSTTR technique considers overall interfacial thermal resistance as a combined effect from discrete components, there are several undetermined interface material properties, such as density, specific heat, thickness, and thermal diffusivity, as indicated in Eq. (10). Some properties are documented and are used as constants through the fitting process, while some other properties, such as thermal conductivity, thermal diffusivity, and contact resistance, remain unknown and need to be determined. When implementing the multi-parameter fitting method, these to-be-determined properties are set to change within certain ranges until a set of values that gives the best fit between the experimental and theoretical data is identified. For the TC-5022 measurement shown in Fig. 5, the thermal diffusivity is 5.44 $\times 10^{-6}$ m^2/s, and the contact resistance of the silicon–TC-5022 interface is 8.19 $mm^2 \cdot K/W$, which represents the single interfacial thermal resistance only. By adopting a density of 3,230 kg/m^3 and a specific heat of 251 J/(kg·K), the thermal conductivity of TC-5022 is calculated to be 4.41 W/(m·K). Because the heat flow is primarily along the thickness direction, based on thermal circuit series assumptions, the overall interfacial thermal resistance is 32.9 $mm^2 \cdot K/W$. It is then concluded that about 50% of the thermal resistance is caused by thermal transport within the material, and the other 50% is from the scattering at the contact surfaces. This measured interfacial thermal resistance is greater than prior measurements in our group using the ASTM method D5470 test method - which was about 25 $mm^2 \cdot K/W$ for 70 μm thick thermal grease layer. [27]. A probable reason for the difference is because the PSTTR measurement is very localized at a small area of about 1- to 2-mm radius and ASTM D5470 is conducted over a much larger area. Therefore, the thermal resistance measured by the ASTM D5470 test method better reflects a region-averaged thermal performance, but the actual resistance still varies from spot to spot. In order to acquire the thermal resistance distribution of the interface, the PSTTR technique should be used to scan the whole surface area. Another possible reason is that we keep applying an external pressure when implementing the ASTM method, which improves the surface contact. The sample tested by PSTTR is mounted in a free condition without exterior pressure. Hence, the surface contact may be affected by the continuous laser heating. However, PSTTR has presented an insight into the interface and reveals that the thermal grease material and contact surfaces induce almost equal impedance to the heat flow. In addition, to eliminate random error from a single measurement, multiple measurements are performed, and the averaged fitted values of the selected parameters are listed in Table 1.

Btech thermoplastic film (HM-2)

Btech thermoplastic film is another TIM that uses highly aligned high-density fibers to conduct heat efficiently. Since the fibers are aligned in the thickness direction, heat transfer is significantly enhanced in the thickness/out-of-plane direction. The overall thickness of the bonded sample is about 370 μm. Measurements of the Btech thermoplastic film-bonded sample are depicted in Fig. 6. The theoretical results are also plotted. The fitted thermal diffusivity is 1.38 $\times$ 10^{-5} m^2/s, and the thermal conductivity is calculated to be 21.15 W/(m·K), when a density of 1,520 kg/m^3 and a specific heat of 1,010 J/(kg·K) are used. The contact resistance is determined to be 2.58 $mm^2 \cdot K/W$. The overall thermal resistance of the thermoplastic layer is calculated to be 8.94 $mm^2 \cdot K/W$, about 60% of which is from the contact resistance. The Btech sample is also studied using the xenon flash technique. The overall interface thermal resistance was measured at around 6 $mm^2 \cdot K/W$, close to the derived values in this work. To eliminate the uncertainty from individual measurements, PSTTR was conducted repeatedly at different positions.

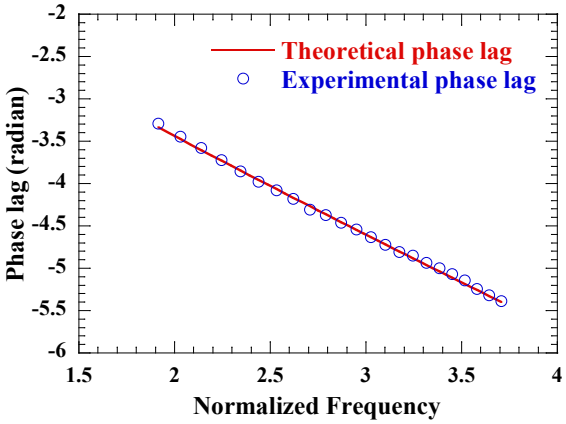

Fig. 5 Experimental and theoretical phase lags as a function of normalized frequency for a silicon-grease-silicon multilayer sample.

The out-of-plane bulk thermal conductivity of the thermoplastic layer was determined to be around 20 to 50 W/(m·K). These values are much higher than most polymers and semiconductors, but are still more than one order of magnitude lower than the out-of-plane thermal conductivity of

HM-2, which is about 700 W/(m·K). This significant reduction is probably caused by the non-ideal bonding quality. The existence of misalignments and imperfections strongly hinders the phonon transport along the thickness direction and causes lower thermal conductivity; however, the total interfacial thermal resistance of Btech HM-2 thermoplastic film is still much lower than that of the thermal grease. If the bonding process is carefully executed to maintain ideal alignment of the graphite fibers, the thermal resistance could be further decreased. This predication makes Btech thermoplastic film an excellent candidate for highly efficient heat removal. Averaged fitted values for key parameters, such as thermal conductivity and contact resistance are derived based on results from multiple measurements, as listed in Table 1.

Diffusion-bonded sample

Diffusion bonding is a novel process that bonds materials without additional intermediate layers. It can be used to bond both metals and nonmetals. Among all applicable materials, silicon is the most established material up to now. The diffusion-bonded sample in this work was provided by our collaborators Delphi, and uses two pre-processed silicon wafers. The thickness is measured to be 200 μm after bonding. To achieve optimal bonding quality, a layer of aluminum about 2 μm thick is sputter coated on each mating surface. Because diffusion bonding is based on atomic interactions, the bonding quality is assumed much improved over conventional bonding materials. In this work, because two thin layers of aluminum are coated, we then consider the interface to be an Al–Al interface. Together with the two silicon wafers, the bonded sample is described as a four-layer structure, which includes four layers of material (silicon, aluminum, aluminum, silicon) and three contact interfaces (Si–Al, Al–Al, Al–Si). The four-layer model is analogous to the three-layer model discussed above, and theoretical solutions are acquired following the same method.

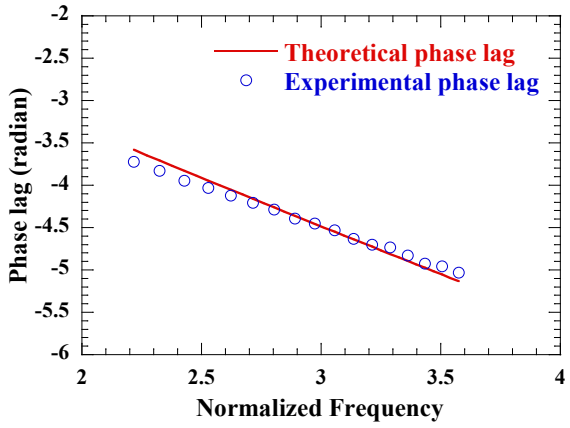

Fig. 6 Experimental and theoretical phase lags as a function of normalized frequency for a sample bonded with Btech HM-2 thermoplastic film.

The phase lag based on four-layer modeling is much more complicated than Eq. (10). Similar to the three-layer heat transfer model, the constant $\pi/4$ term and phase lags from the thermal wave traveling in each layer remain the same. However, the number of interfaces brings greater complexity into the solution. Nevertheless, patterns related to the effusivities and resistances are noticeable, similar to that indicated in the phase lag solutions in the theoretical modeling section. A four-layer solution is then validated by its reducibility to Eq. (10), Eq. (12), and Eq. (11) using appropriate assumptions.

With a four-layer phase solution, the multi-parameter fitting method is performed. Both experimental and theoretical phase lags are presented in Fig. 7. Based on the fit, the thermal resistance is determined to be 0.53 $mm^2 \cdot K/W$. To be more specific, the contact resistance between silicon and aluminum surfaces is about 0.08 $mm^2 \cdot K/W$. According to work reported on solid interfaces, room-temperature contact resistances between metals and dielectrics are about 0.01 to 0.1 $mm^2 \cdot K/W$. [29, 30] In addition, the thermal resistance of the 2-μm aluminum coating is less than 0.01 $mm^2 \cdot K/W$, which is negligible compared to that of other components. The Al–Al interface contact resistance is fitted to be 0.34 $mm^2 \cdot K/W$, meaning that over 60% of the thermal resistance is caused by this interface. The contact resistance is mainly caused by phonon/electron scattering at the interface and also the ambient imperfections, such as voids and dislocations. Because the aluminum layer is sputter coated, the adhesion is optimal. In addition, the coated aluminum layer has ultra-fine and highly uniform surface features. In comparison, when the two silicon layers are bonded at elevated temperature and additional pressure, the surfaces do not adhere as well as a sputter-coated surface. Therefore, the resistance from an Al–Al interface emerges as stronger impedance to the heat flow. Upon several measurements, the averaged values for the two contact resistances are presented in Table 2. The interfacial thermal resistance of the diffusion-bonded silicon wafers is impressively low compared with the thermal resistances in Table 1.

Table 2. Parameters of diffusion-bonded sample.

Parameters	Value
Total Thickness (μm)	200
Bondline thickness (μm)	4.00
Density of Aluminum (kg/m^3)	2,700
Specific heat of Aluminum ($J/(kg \cdot K)$)	900
Thermal conductivity of Aluminum ($W/(m \cdot K)$)	205
Thermal diffusivity of Aluminum ($\times 10^{-5}$ m^2/s)	8.40
Al–Si contact resistance ($mm^2 \cdot K/W$)	0.06
Al–Al Contact resistance ($mm^2 \cdot K/W$)	0.33
Overall thermal resistance ($mm^2 \cdot K/W$)	0.47

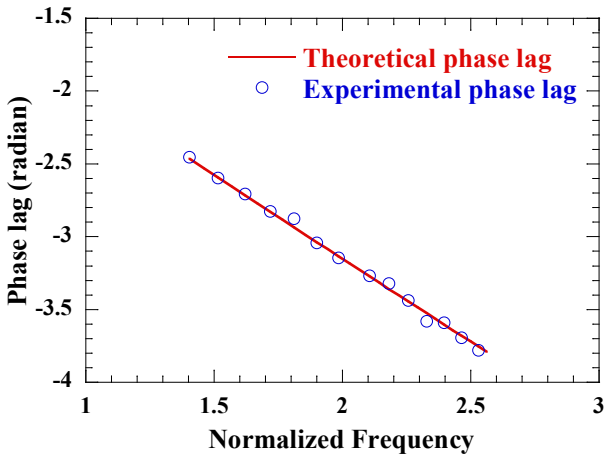

Fig. 7 Experimental and theoretical phase lags as a function of normalized frequency for the diffusion-bonded sample.

Measurement sensitivity

To achieve effective measurements, a study of sensitivity of the output signal to parameters is necessary. The greater the change in output signal due to changes in particular parameters is, the more accurately the parameter is determined. Graphic presentations of the sensitivity of critical parameters for the samples measured are shown in Fig. 8. For all three plots in Fig. 8, in addition to the experimental and theoretical curves, several other curves obtained by varying relevant parameters to certain levels are also included. Fig. 8(a) shows how much the phase lag changes from the best fit curve upon ±10% change in thermal diffusivity. Distinct deviations are observed in this figure when thermal diffusivity is either enhanced or reduced by 10%. This suggests that the phase lag is sensitive to thermal diffusivity and the fitted value of thermal diffusivity is accurate enough. It is also seen that when the frequency increases, the deviation from the theoretical curve is greater. This suggests that the sensitivity is also related to the frequency. If a higher sensitivity needs to be achieved, an appropriate frequency range is required. The sensitivity curves of TC-5022 and Btech HM-2 are shown in Figs. 8(b) and 8(c), respectively. Using variations of 20%, the thermal conductivity and thermal resistance show drastically different influences on the system sensitivity. The curves with ±20% thermal resistance are very close to the best fit curve, while curves with ±20% thermal conductivity significantly depart from the best fit curve. Insets in both Figs. 8(b) and 8(c) show this difference more clearly.

As stated, it is seen that the deviation from the theoretical curves upon certain variations of the parameters is not constant through the frequency range. Therefore, if we understand how sensitivity is qualitatively related to the frequency, it is instructive for us to determine the proper frequency to be used in the measurements. The sensitivity of a measurement output to a specific parameter is quantitatively expressed as the partial derivative of the function over that parameter, namely, df/db, in which f is the output signal and b is the experimental parameter.

For single silicon wafer materials, based on Eq. (3), the sensitivity of the phase lag on the thermal diffusivity is expressed as:

$$|\Delta\emptyset| = \left|\left(\frac{d\emptyset}{d\alpha}\right)\cdot\Delta\alpha\right| = \left|\frac{b\cdot\sqrt{\pi f}}{2}\alpha^{-\frac{3}{2}}\cdot\Delta\alpha\right| \qquad (13)$$

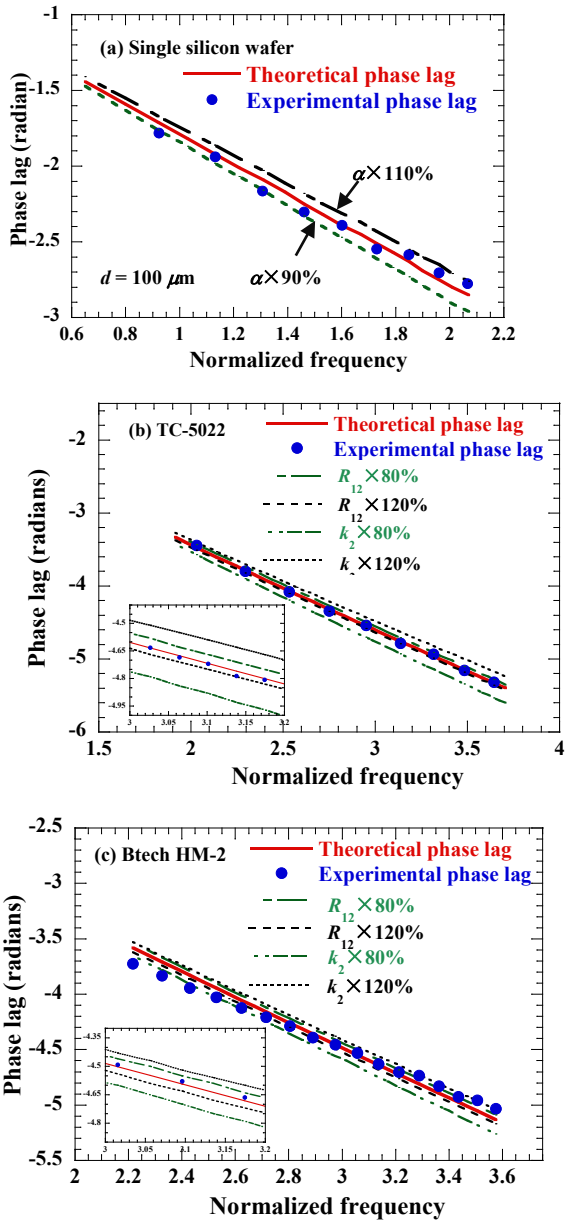

Fig. 8 (a) Calculated phase lag curve changes for the single silicon wafer data on ±10% changes in thermal diffusivity α around the best fit value; (b) Calculated phase lag curve changes for TC-5022 bonded sample upon ±20% changes in bulk thermal conductivity, k, and contact resistance, R, around the best fit value; (c) Calculated phase lag curve changes for Btech HM-2 bonded sample upon ±20% changes in bulk thermal conductivity, k, and contact resistance, R, around the best fit value. Insets in (b) and (c) are partial enlarged images to more distinctly show the deviations from best fit curves upon certain changes in the fitted parameters.

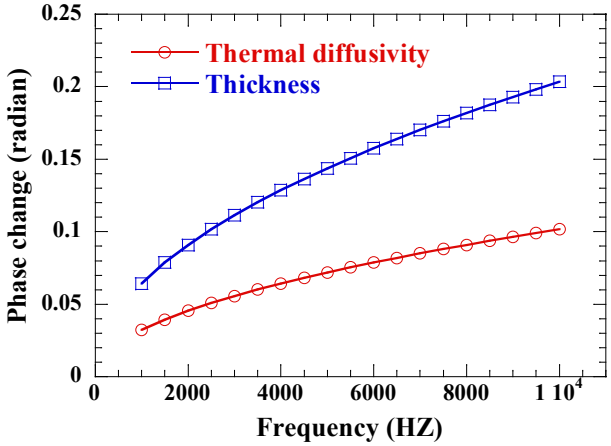

Fig. 9 Absolute values of phase changes in a silicon wafer as a function of frequency with respect to a 10% change in thermal diffusivity and thickness.

So, when the thermal diffusivity is set to vary by 10%, namely, $\Delta\alpha$ is α ×10%, the change in the phase lag is a function of frequency as described by Eq. (13). Greater change in phase indicates it has greater sensitivity to the thermal diffusivity α. Therefore, from Fig. 9, the phase lag for a single silicon wafer is more sensitive to thickness than to the thermal diffusivity. The sensitivity of phase lag to both parameters increases with frequency.

For both thermal grease and Btech thermoplastic film measurements, three-layer heat transfer modeling is applied and a multi-parameter fitting technique is used to find a set of parameters that yield the best fit. Because multiple parameters are of interest in three-layer samples, the sensitivity of the phase lag to each parameter is investigated separately. Because of the structural symmetry, the two contact resistances are actually interchangeable, so the sensitivities of phase lag to both R_{12} and R_{23} are equal. The phase change in absolute value upon a 10% change of these parameters is plotted in Fig. 10. Because of the correlation between thermal conductivity and thermal diffusivity, only the sensitivity curve to thermal conductivity is shown. It is clearly observed that when the modulation frequency increases, the phase change is more sensitive to thermal conductivity than to contact resistance. In addition, the sensitivities to both contact resistances are identical, as stated above.

Uncertainty analysis

When conducting the PSTTR experiment, environmental noise and disturbance may introduce errors into the phase measurement. To further estimate the uncertainty in the parameters due to the errors in phase measurement, error propagation equation is employed here, as defined below:

$$\frac{\Delta f}{f} = \frac{1}{f} \cdot \left| \frac{\partial f}{\partial x_i} \cdot \Delta x_i \right| \tag{14}$$

Therefore, for a single silicon wafer, if the error in thermal diffusivity is of concern, it is then modified into a function of phase,

$$\frac{\Delta\alpha}{\alpha} = \frac{1}{\alpha} \cdot \left| \frac{\partial\alpha}{\partial\phi} \cdot \Delta\phi \right| = \left| \frac{2}{\phi - \frac{\pi}{4}} \cdot \Delta\phi \right| \tag{15}$$

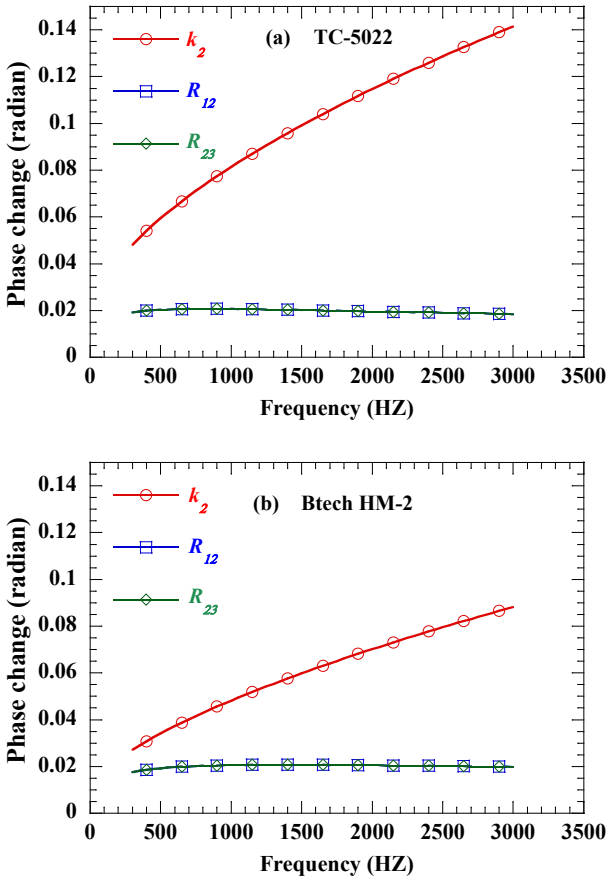

Fig. 10 Absolute values of phase changes of (a) TC-5022 and (b) Btech HM-2 bonded sample as a function of frequency with respect to a 10% change in thermal conductivity k and contact resistance R.

Here, $\Delta\phi$ is the error in phase readings from the lock-in amplifier; which is about 5 degrees (0.08 radians). Hence, the percentage error in the derived thermal diffusivity is estimated to be from 8% to 19%, depending on the frequency range chosen for measurement. At higher frequencies, the percentage error approaches the lower end of about 8%, meaning that high frequency reduces the uncertainty. This is also supported by the sensitivity analysis in the previous section. For a single silicon wafer, the sensitivity of phase measurement to thermal diffusivity gets greater when frequency increases, as shown in Fig. 9. Therefore, high frequency is required in PSTTR measurement, not only to derive the theoretical solutions, but also to ensure high sensitivity and low measurement uncertainty. Because the uncertainty changes with frequency selected in measurement, a mean uncertainty of 13% is selected for thermal diffusivity α for a single silicon wafer. To further derive the uncertainty for thermal conductivity, errors in density ρ and specific heat c_p are required. Because silicon is a well-studied material, the errors for density and specific heat are assumed to be 1%. Therefore, the uncertainty for the thermal conductivity k based on error propagation theory is 13%.

For thermal grease TC-5022 and Btech HM-2 thermoplastic film, uncertainty analysis in the thermal conductivity k and

thermal resistance R is conducted using the same methodology. Details are not included here. Following the same process for thermal grease TC-5022, the error for thermal conductivity is determined to be 10% and that for contact resistance is 35%. Therefore, the uncertainty for overall thermal resistance is about 17%. For Btech HM-2 thermoplastic film, the error for thermal conductivity, contact resistance, and overall thermal resistance are 18%, 35%, and 25%, respectively. Uncertainty values for these particular parameters are also indicated after the "±" symbols in Table 1. The comparison of uncertainties for different parameters indicates that contact resistance contains larger uncertainty than thermal conductivity because the measurement sensitivity to contact resistance is lower, as analyzed above.

CONCLUSION

The PSTTR technique is applied to study the thermal properties of various types of TIMs. A phase lag–frequency profile is obtained, and then a multi-parameters fitting process is employed to find the targeted parameters by identifying the best fit between the experimental data and theoretical calculations. The TIMs studied in this work include a conventional thermal grease (TC-5022), Btech HM-2 thermoplastic film, and diffusion-bond silicon wafers. While traditional techniques such as ASTM D5470 and laser flash are not capable of differentiating sources of thermal resistance within the interfacial layer, or for measuring thermal resistances below 1 $mm^2 \cdot K/W$, PSTTR provides valuable information to understand the interface thermal resistance by deriving both the bulk thermal conductivity of the material itself and thermal resistance of the surfaces in contact simultaneously. Using the PSTTR measurements, the bulk thermal conductivity of Dow Corning's TC-5022 thermal grease (70–75 μm BLT) was 3 to 5 W/(m·K), and the contact resistance was 5 to 10 $mm^2 \cdot K/W$. Due to the nature of thermal grease, the thermal conductivity from fillers can be further improved to reduce the interfacial thermal resistance. For Btech HM-2 thermoplastic material (45–80 μm BLT), the bulk thermal conductivity was from 20 to 40 W/(m·K), and the contact resistance was about 2 to 5 $mm^2 \cdot K/W$. Because the Btech thermoplastic film is synthesized from highly aligned graphite fibers, most of the impedance to heat flow comes from surface contact. A sample fabricated using high-thermal-performance diffusion bonding was also measured in this work. Compared with samples prepared using interfacial materials, the thermal resistance of the diffusion-bond sample is lower than 1 $mm^2 \cdot K/W$, varying from 0.3 to 0.6 $mm^2 \cdot K/W$. While there are metal–metal and metal–dielectric interfaces, most of the thermal resistance is from the Al–Al interface, the contact resistance of which is about one order of magnitude greater than that of the Al–Si interface. Because the aluminum layer is sputter-coated, adhesion between aluminum and silicon is excellent compared with the bonding quality of an Al–Al interface. Comparison among these TIMs implies that diffusion bonding is the most promising technique that causes the lowest thermal resistance to heat flow. The thermal performance of thermoplastics is also very good. Prior work [27] has shown that when the thermal resistance of the interface materials is below 5 $mm^2 \cdot K/W$, they will stop being a bottleneck to heat removal in most power electronics packaging applications. While the thermal performance of the diffusion-bonded interface is outstanding (< 1 $mm^2 \cdot K/W$), thermoplastics are also very good potential candidates for application in advanced low-resistance power electronics packaging configurations.

ACKNOWLEDGMENTS

The authors would like to acknowledge the support provided by Susan Rogers and Steven Boyd, Technology Development Managers for Advanced Power Electronics and Electric Motors, Vehicle Technologies Office, U.S. Department of Energy Office of Energy Efficiency and Renewable Energy. The authors would like to acknowledge Doug DeVoto and Mark Mihalic (NREL) for synthesizing the bonded samples based on the Btech material, Jay Browne (Btechcorp) for providing the thermoplastic material, as well as Ralph Taylor (Delphi) for providing the diffusion-bonded sample.

REFERENCES

[1] D. D. L. Chung, "Thermal interface materials," *Journal of Materials Engineering and Performance,* vol. 10, no. 1, pp. 56-59, Feb, 2001.

[2] J. Due, and A. J. Robinson, "Reliability of thermal interface materials: A review," *Applied Thermal Engineering,* vol. 50, no. 1, pp. 455-463, Jan, 2013.

[3] J. P. Gwinn, and R. L. Webb, "Performance and testing of thermal interface materials," *Microelectronics Journal,* vol. 34, no. 3, pp. 215-222, Mar, 2003.

[4] A. J. McNamara, Y. Joshi *et al.*, "Characterization of nanostructured thermal interface materials - A review," *International Journal of Thermal Sciences,* vol. 62, pp. 2-11, Dec, 2012.

[5] K. C. Otiaba, N. N. Ekere *et al.*, "Thermal interface materials for automotive electronic control unit: Trends, technology and R&D challenges," *Microelectronics Reliability,* vol. 51, no. 12, pp. 2031-2043, Dec, 2011.

[6] R. Prasher, "Thermal interface materials: Historical perspective, status, and future directions," *Proceedings of the Ieee,* vol. 94, no. 8, pp. 1571-1586, Aug, 2006.

[7] Z. R. Liu, and D. D. L. Chung, "Calorimetric evaluation of phase change materials for use as thermal interface materials," *Thermochimica Acta,* vol. 366, no. 2, pp. 135-147, Jan, 2001.

[8] Y. Aoyagi, C. K. Leong *et al.*, "Polyol-based phase-change thermal interface materials," *Journal of Electronic Materials,* vol. 35, no. 3, pp. 416-424, Mar, 2006.

[9] Y. Aoyagi, and D. D. L. Chung, "Antioxidant-based phase-change thermal interface materials with high thermal stability," *Journal of Electronic Materials,* vol. 37, no. 4, pp. 448-461, Apr, 2008.

[10] A. P. Yu, P. Ramesh *et al.*, "Graphite nanoplatelet-epoxy composite thermal interface materials," *Journal of Physical Chemistry C,* vol. 111, no. 21, pp. 7565-7569, May, 2007.

[11] R. Cross, B. A. Cola *et al.*, "A metallization and bonding approach for high performance carbon nanotube thermal interface materials," *Nanotechnology,* vol. 21, no. 44, Nov, 2010.

[12] C. J. Lasance, "The urgent need for widely-accepted test methods for thermal interface materials," *Semiconductor Thermal Measurement and Management Symposium, 2003. Ninteenth Annual IEEE.* pp. 123-128, 2003.

[13] "American Society for Testing and Materials, ASTM Standard D5470-01," 2005.

[14] J. Culham, P. Teertstra *et al.*, "Design, assembly and commissioning of a test apparatus for characterizing thermal interface materials," *ITHERM 2002. The Eighth Intersociety Conference on Thermal and Thermomechanical Phenomena in Electronic Systems.* pp. 128-135, 2002.

[15] J. Xu, and T. S. Fisher, "Enhancement of thermal interface materials with carbon nanotube arrays," *International Journal of Heat and Mass Transfer,* vol. 49, no. 9-10, pp. 1658-1666, May, 2006.

[16] C. I. Chen, C. Y. Ni *et al.*, "Thermal characterization of thermal interface materials," *Experimental Techniques,* vol. 32, no. 3, pp. 48-52, May-Jun, 2008.

[17] X. H. Feng, and X. W. Wang, "Thermophysical properties of free-standing micrometer-thick Poly (3-hexylthiophene) films," *Thin Solid Films,* vol. 519, no. 16, pp. 5700-5705, Jun, 2011.

[18] X. H. Feng, X. P. Huang *et al.*, "Thermal conductivity and secondary porosity of single anatase TiO2 nanowire," *Nanotechnology,* vol. 23, no. 18, May, 2012.

[19] X. H. Feng, X. P. Huang *et al.*, "Nonlinear effects in transient electrothermal characterization of anatase TiO2 nanowires," *Review of Scientific Instruments,* vol. 83, no. 4, Apr, 2012.

[20] X. H. Feng, G. Q. Liu *et al.*, "3-dimensional anisotropic thermal transport in microscale poly(3-hexylthiophene) thin films," *Polymer,* vol. 54, no. 7, pp. 1887-1895, Mar, 2013.

[21] C. A. Paddock, and G. L. Eesley, "Transient Thermoreflectance from Metal-Films," *Optics Letters,* vol. 11, no. 5, pp. 273-275, May, 1986.

[22] G. L. Doll, G. L. Eesley *et al.*, "Transient-Thermoreflectance Study of Single-Crystal Lanthanum Cuprate," *Physical Review B,* vol. 40, no. 13, pp. 9354-9357, Nov, 1989.

[23] Y. Ohsone, G. Wu *et al.*, "Optical measurement of thermal contact conductance between wafer-like thin solid samples," *Journal of Heat Transfer-Transactions of the Asme,* vol. 121, no. 4, pp. 954-963, Nov, 1999.

[24] P. L. Komarov, and P. E. Raad, "Performance analysis of the transient thermo-reflectance method for measuring the thermal conductivity of single layer materials," *International Journal of Heat and Mass Transfer,* vol. 47, no. 14-16, pp. 3233-3244, Jul, 2004.

[25] H. K. Lyeo, and D. G. Cahill, "Thermal conductance of interfaces between highly dissimilar materials," *Physical Review B,* vol. 73, no. 14, Apr, 2006.

[26] T. Tong, Y. Zhao *et al.*, "Dense, vertically aligned multiwalled carbon nanotube arrays as thermal interface materials," *Ieee Transactions on Components and Packaging Technologies,* vol. 30, no. 1, pp. 92-100, Mar, 2007.

[27] S. Narumanchi, M. Mihalic *et al.*, "Thermal interface materials for power electronics applications," *ITHERM 2008. 11th Intersociety Conference on Thermal and Thermomechanical Phenomena in Electronic Systems. .* pp. 395-404, 2008.

[28] F. P. Incropera, A. S. Lavine *et al.*, *Fundamentals of heat and mass transfer*, 3rd ed.: John Wiley & Sons Incorporated, New York, 2011.

[29] O. W. Kading, H. Skurk *et al.*, "Thermal Conduction in Metallized Silicon-Dioxide Layers on Silicon," *Applied Physics Letters,* vol. 65, no. 13, pp. 1629-1631, Sep, 1994.

[30] P. L. Komarov, M. G. Burzo *et al.*, "Transient thermo-reflectance measurements of the thermal conductivity and interface resistance of metallized natural and isotopically-pure silicon," *Microelectronics Journal,* vol. 34, no. 12, pp. 1115-1118, Dec, 2003.